



Cite this: *Nanoscale*, 2025, **17**, 10013

## Epitaxial growth of antiferromagnetic $\text{MnBi}_2\text{Te}_4/\text{CdTe}$ heterostructures on $\text{GaAs}(001)$ using molecular beam epitaxy: structure and electronic properties

Wesley F. Inoch,<sup>a</sup> Gilberto Rodrigues-Junior,<sup>a</sup> S. L. A. Mello,<sup>a</sup> S. de Castro,<sup>b</sup> M. L. Peres,<sup>b</sup> Sukarno O. Ferreira,<sup>a</sup> Ângelo Malachias,<sup>a</sup> Maybi F. Sampaio,<sup>d</sup> Olavo Teixeira Neto,<sup>d</sup> Bráulio S. Archanjo<sup>d</sup> and Leonarde N. Rodrigues<sup>a</sup>    

$\text{MnBi}_2\text{Te}_4$  is one of the most recent materials that integrates the class of topological quantum materials exhibiting topological insulating properties and magnetic ordering, thus providing the opportunity to investigate particular topological quantum states and design novel spintronic devices. The samples were grown on  $\text{GaAs}(100)$  substrates using molecular beam epitaxy with  $\text{Bi}_2\text{Te}_3$ ,  $\text{Te}$  and  $\text{Mn}$  as sources. The growth was characterized through X-ray diffraction, atomic force microscopy and transmission electron microscopy. Topological insulator properties were probed through scanning tunneling microscopy and scanning tunneling spectroscopy, while antiferromagnetic order was investigated via magnetotransport measurements. Furthermore, we propose a high-quality  $\text{CdTe}$  thin film as a cap layer to protect topological surface states, thus opening the possibility of integrating topological quantum materials with group II–VI semiconductors *via* van der Waals epitaxy.

Received 30th November 2024,  
Accepted 8th March 2025

DOI: 10.1039/d4nr05042h  
[rsc.li/nanoscale](http://rsc.li/nanoscale)

## Introduction

Novel materials exhibiting exotic states of matter, such as topological insulators (TIs), have attracted considerable attention in solid-state physics in the last decades.<sup>1</sup> The quantum spin Hall effect observed in  $\text{HgTe}$  quantum wells<sup>2</sup> grown *via* molecular beam epitaxy (MBE) confirmed typical TI behavior with protected conductor surface states due to spin-orbit coupling and time-reversal symmetry. Such characteristics make this material a promising candidate for sophisticated spintronic devices and quantum computation applications.<sup>3</sup> In recent years, the combination of topological insulation properties with magnetic ordering has enabled the emergence of a new class of topological quantum materials.<sup>4</sup> The magnetic moment provides mass to the otherwise massless Dirac fermions, thus opening an energy gap and allowing topologically

driven quantum states to emerge in the system.<sup>5</sup> Exotic states of matter such as quantum anomalous Hall effect (QAHE)<sup>6</sup> insulators and axion insulators<sup>7</sup> have been observed as a response to the coexistence between magnetism and topological insulator state.

Magnetically doped topological insulators, such as Cr- and V-doped  $(\text{Bi},\text{Sb})_2\text{Te}_3$ , present the QAHE.<sup>8</sup> However, the temperature to measure the effect is  $<1$  K owing to structural defects in the  $\text{Bi}_2\text{Te}_3$  crystal introduced by dopants. Magnetic topological insulators such as  $\text{MnBi}_2\text{Te}_4$  with antiferromagnetic order<sup>9</sup> are an alternative to magnetically doped TIs since they are expected to exhibit the QAHE at relatively high temperatures, thus enabling device applications. The QAHE has also been predicted for thin films/flakes of  $\text{MnBi}_2\text{Te}_4$ -family compounds.<sup>10</sup>

Quantum transport properties of  $\text{MnBi}_2\text{Te}_4$  have been exploited to achieve the QAHE at zero magnetic field in thin film samples grown *via* MBE.<sup>9</sup> Recently, a study addressed QAHE results<sup>11</sup> to clarify the controversial data available. Although the QAHE has been reported in thin flakes<sup>6</sup> of  $\text{MnBi}_2\text{Te}_4$  and giant nonlocal transport signals in the axion insulator state,<sup>12</sup> a thin film grown *via* MBE does not present limitations with the control in the fabrication of the film shape and does not have the size limitation as in the case of exfoliated flakes. The reproducibility and control of composition and thickness positions the MBE growth technique as

<sup>a</sup>Departamento de Física, Instituto de Ciências Exatas (ICE), Universidade Federal de Viçosa, Viçosa, Minas Gerais 36570-900, Brasil. E-mail: leonarde.rodrigues@ufv.br

<sup>b</sup>Instituto de Física e Química, Universidade Federal de Itajubá, Itajubá, Minas Gerais 37500-903, Brasil

<sup>c</sup>Departamento de Física, Instituto de Ciências Exatas (ICE), Universidade Federal de Minas Gerais (UFMG), Av. Antônio Carlos, 6627, Belo Horizonte, Minas Gerais 30123-970, Brasil

<sup>d</sup>Instituto Nacional de Metrologia, Qualidade e Tecnologia (Inmetro), Divisão de Materiais (DIMAT), Xerém, 25250-020 Rio de Janeiro, Brasil

an appropriate choice to achieve the fabrication of large-area and high-quality topological magnetic devices.<sup>9,11</sup> Previous works in this field have been performed using the MBE growth of  $\text{MnBi}_2\text{Te}_4$  on different substrates such as  $\text{BaF}_2(111)$ ,<sup>13</sup> sapphire(0001),<sup>11</sup>  $\text{Si}(111)$ ,<sup>14</sup>  $\text{Al}_2\text{O}_3(0001)$ ,<sup>15</sup>  $\text{SrTiO}_3(111)$ <sup>16</sup> and  $\text{GaAs}(111)\text{B}$ .<sup>17</sup> A common link between these works is the use of two effusion cells containing  $\text{Bi}_2\text{Te}_3$  and  $\text{MnTe}$  or three effusion cells containing  $\text{Te}$ ,  $\text{Bi}$  and  $\text{Mn}$ . The former<sup>13</sup> basically controls the beam equivalent pressure between  $\text{Bi}_2\text{Te}_3$  and  $\text{MnTe}$ . Other works,<sup>15,17</sup> since  $\text{MnBi}_2\text{Te}_4$  is sensitive to the  $\text{Bi}:\text{Mn}$  flux ratio, provide the fine stoichiometry tuning of  $\text{MnBi}_2\text{Te}_4$ , controlling each source individually. Some approaches may follow a more complex routine involving growth and annealing of a  $\text{Bi}_2\text{Te}_3$  buffer layer.<sup>17</sup>

Although van der Waals (vdW) material growth conditions are challenging considering weak interlayer forces, good quality systems can be grown *via* MBE, despite the large lattice mismatch between the film and substrate.<sup>18</sup> Careful control of growth conditions is necessary for the formation of correct stoichiometry and phase. In this work,  $\text{MnBi}_2\text{Te}_4$  thin films were directly grown on a  $\text{GaAs}(001)$  substrate using molecular beam epitaxy.  $\text{GaAs}$  is a suitable substrate choice used in spintronics and can be a platform for integrating topological insulator devices.<sup>19</sup> The growth recipe used here is similar to that reported previously<sup>20</sup> for the growth of  $\text{Bi}_2\text{Te}_3$  using one additional  $\text{Mn}$  effusion cell. This versatile control can allow the growth of heterostructures and superstructures such as  $\text{Bi}_2\text{Te}_3/\text{MnBi}_2\text{Te}_4$  with only three effusion cells. To avoid the exposure of topological insulators to air and prevent the degradation of surface states, we grew a  $\text{CdTe}$  cap layer on top of the  $\text{MnBi}_2\text{Te}_4$  film, substituting the usually used  $\text{Te}$  cap because the metallic  $\text{Te}$  layer would work as a transport channel, masking the transport that occurs through the  $\text{MnBi}_2\text{Te}_4$  film.<sup>21</sup> This high-resistivity  $\text{CdTe}$  layer opens the possibility to integrate TIs with II-VI heterostructures. The morphological and structural properties of  $\text{MnBi}_2\text{Te}_4$  are characterized using

atomic force microscopy (AFM), high resolution X-ray diffraction (HRXRD) and high-resolution transmission electron microscopy (HRTEM). Topological surface state properties were studied using scanning tunneling spectroscopy (STS), thus providing information about the surface local density of states (LDOS). To verify the antiferromagnetic order and electronic properties of  $\text{MnBi}_2\text{Te}_4$ , magnetoresistance and van der Pauw measurements were conducted.

## Experimental

$\text{Bi}_2\text{Te}_3$  and  $\text{MnBi}_2\text{Te}_4$  were grown using a custom-built molecular beam epitaxy (MBE) system on undoped  $\text{GaAs}(001)$  substrates. Before growth, the substrate was annealed at 580 °C for 5 min to completely remove native oxide. Standard effusion cells containing high-purity powders of  $\text{Bi}_2\text{Te}_3$ ,  $\text{Te}$ ,  $\text{Mn}$ , and  $\text{CdTe}$  were used for growth. Growth parameters were the same as those already reported<sup>20</sup> for the growth of  $\text{Bi}_2\text{Te}_3$ , with the addition of a  $\text{Mn}$  source. Unlike previously mentioned works on the growth of  $\text{MnBi}_2\text{Te}_4$  on different substrates, our growth recipe uses independent sources of  $\text{Bi}_2\text{Te}_3$ ,  $\text{Te}$  and  $\text{Mn}$ . The same beam fluxes of  $\text{Bi}_2\text{Te}_3$  and  $\text{Te}$  were maintained by adjusting the same deposition rate grown at room temperature and measuring the thickness of pure  $\text{Bi}_2\text{Te}_3$  and  $\text{Te}$  films. The  $\text{MnBi}_2\text{Te}_4$  structure (deposition rate of approximately 0.5 nm min<sup>-1</sup>) was reached using pure  $\text{Mn}$  evaporated from an effusion cell with an optimized temperature of 840 °C. The substrate temperature used was 380 °C for  $\text{MnBi}_2\text{Te}_4$  and  $\text{CdTe}$  thin films. High-purity polycrystalline  $\text{CdTe}$  was evaporated from single effusion cells with a deposition rate of approximately 3 nm min<sup>-1</sup>. The base pressure never exceeded 10<sup>-8</sup> Torr.  $\text{Bi}_2\text{Te}_3$  samples were grown for comparison. To avoid the exposure of the topological insulator to air, we grew an undoped 60 nm-thick  $\text{CdTe}$  cap layer on top of the  $\text{MnBi}_2\text{Te}_4$  film. The crystalline structure of the  $\text{Bi}_2\text{Te}_3$  and  $\text{MnBi}_2\text{Te}_4$  films was investigated through high-resolution X-ray diffraction (HRXRD) using a four-circle Bruker D8-discover diffractometer equipped with  $\text{Cu K}\alpha$  ( $\lambda = 1.54056$  Å) radiation source and a 2-bounce Ge (220) monochromator. The deposition rate and interface roughness were estimated using X-ray reflectometry (XRR) measurements. XRR fits using the Parratt formalism<sup>22</sup> or the available algorithm<sup>23</sup> allows the evaluation of the layer thickness and interface roughness of the deposited layer. AFM measurements were carried out using a FlexAFM Nanosurf microscope operating in a tapping (semi-contact) mode with controlled humidity maintained below 30%. Cross-sectional focused ion beam (FIB) thin lamellae were prepared using an FEI Helios Nanolab 650 DualBeam system, with final polishing conducted at 2 keV and a 7° tilt to minimize amorphization caused by the Ga FIB. Scanning transmission electron microscopy (STEM) was performed using a Cs probe-corrected Titan 80-300 (FEI Company) transmission electron microscope operating at 300 kV. The microscope was equipped with a conventional high-angle annular dark-field (HAADF) detector and an Oxford Aztec Energy TEM advanced microana-



Leonarde N. Rodrigues

*Leonarde do Nascimento Rodrigues received his doctoral degree from Federal University of Juiz de Fora, Juiz de Fora, Brazil, in 2016. He is currently Professor in the Physics Department at the Federal University of Viçosa, Brazil. His main current research area is the conventional epitaxial growth of semiconductor heterostructures and thin films, van der Waals epitaxial growth of chalcogenide materials, fabrication of semiconductor nanomembranes and devices and their characterization via high resolution X-ray diffraction and optical spectroscopy for inelastic light scattering and photoluminescence applications.*

lysis system. STM and STS measurements were performed under ultra-high vacuum conditions in an Omicron-VT STM system operating at room temperature, with a base pressure of  $1.0 \times 10^{-10}$  mbar. All STM images were acquired using electrochemically etched polycrystalline W tips in a constant current mode, and for STS measurements, a lock-in amplifier (operating a 3000 Hz) was used to obtain differential conductance ( $dI/dV$ ) curves. All STS curves considered here were an average of at least 30 curves taken at the same point. For STS measurements, the samples were capped with Te and immediately exfoliated in vacuum before STS measurements. For magnetotransport measurements, electrical contacts in the van der Pauw geometry were soldered using indium droplets. This procedure was performed using a hot plate at 180 °C for 2 min to guarantee that the diffusion occurs through the layers. The measurements were carried out using the physical properties measurement system (PPMS) from Quantum Design, equipped with a helium-cooled superconducting system with a magnetic field of up to 9 T that operates over a broad temperature range from 1.9 to 400 K. A standard four-probe AC lock-in technique with a constant excitation current of 10  $\mu$ A was employed.

## Results and discussion

Fig. 1(a) and (e) show the XRR data for  $\text{Bi}_2\text{Te}_3$  and  $\text{MnBi}_2\text{Te}_4$  thin films without the CdTe cap layer, with experimental data shown as a black circle and the fitting curve as a blue line. Both samples exhibited well-defined fringes, indicating a uniform film thickness and smooth surface and interface across the substrate area. The model parameters yielded a  $\text{Bi}_2\text{Te}_3$  film thickness of 47.3 nm and surface roughness of 2.6 nm. The  $\text{MnBi}_2\text{Te}_4$  film had a similar thickness of 48.2 nm with a surface roughness of approximately 10% smaller than  $\text{Bi}_2\text{Te}_3$ . The comparable film thickness resulted from using the same growth time and parameters for the  $\text{Bi}_2\text{Te}_3$  and Te effusion cells. The fitting curves were obtained using the bulk material density, and results were in good agreement with experimental results, suggesting that a stoichiometric phase was achieved.

Fig. 1(b) and (f) show symmetrical HRXRD scans for 47 nm  $\text{Bi}_2\text{Te}_3$  and 48 nm  $\text{MnBi}_2\text{Te}_4$  thick films, respectively. In addition to the peaks belonging to the GaAs substrate, it is possible to observe only the (0 0 3n) peaks as labeled in the figure, indicating that both films grew epitaxially on the GaAs substrate. Fig. 1(c) and (g) show the reciprocal space maps (RSMs) acquired near the symmetric  $\text{Bi}_2\text{Te}_3$  (006) and  $\text{MnBi}_2\text{Te}_4$  (009) diffraction peak, respectively, and the (002) diffraction peak of the GaAs as a reference (indicated by the circle). Note that the (002) diffraction peak of GaAs is a nearly perfect single crystal, which reflects the discrepancy between the width of the  $\text{Bi}_2\text{Te}_3$  and  $\text{MnBi}_2\text{Te}_4$  films and the GaAs substrate as can be observed on the RSM around GaAs (002) in Fig. 1(d) and (h). The vertical alignment between the  $\text{Bi}_2\text{Te}_3$  and  $\text{MnBi}_2\text{Te}_4$  films and GaAs indicates well-oriented growth with reflections in the (003n) parallel plane. The distortion of

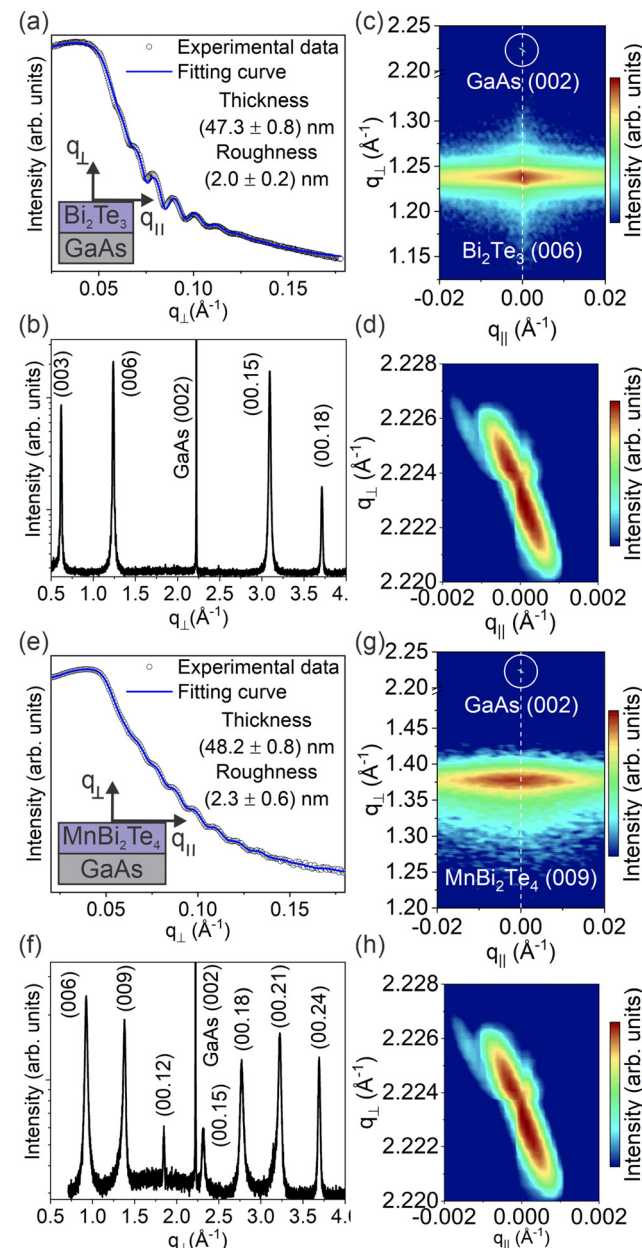


**Fig. 1** Structural comparison of  $\text{Bi}_2\text{Te}_3$  and  $\text{MnBi}_2\text{Te}_4$  Tl. (a) and (e): XRR spectra for  $\text{Bi}_2\text{Te}_3$  and  $\text{MnBi}_2\text{Te}_4$ . Black circles represent the experimental data, while blue lines represent the fitting curve. (b) and (f): HRXRD measurements for the [0001] direction for  $\text{Bi}_2\text{Te}_3$  and  $\text{MnBi}_2\text{Te}_4$ . (c) and (g): reciprocal space mapping around  $\text{Bi}_2\text{Te}_3$ (006) and  $\text{MnBi}_2\text{Te}_4$ (009) reflections and GaAs(002) as a reference indicated by a circle. (d) and (h) Show the RSM around GaAs(002) from (c) and (g), respectively.

GaAs reflection on the RSM originates from the resolution limit of the equipment. The out-of-plane direction reveals symmetric oscillation patterns that confirm the smooth surfaces and a well-ordered structure. In-plane direction has an intense diffuse scattering, indicating the presence of defects in the structure, such as mosaicity, due to the large lattice mismatch. The out-of-plane direction of the  $\text{MnBi}_2\text{Te}_4$ (009) RSM, shown

in Fig. 1(g), is asymmetric with a more pronounced broadening at lower values of reciprocal space. The in-plane diffraction has a FWHM that is twice as large as that of  $\text{Bi}_2\text{Te}_3$ , indicating a larger defect density. Stacking errors may be responsible for the asymmetric behavior and the broadening of the diffraction peaks.

Fig. 2(a, b) and (e, f) shows AFM images ( $5 \times 5 \mu\text{m}^2$ ) and ( $1 \times 1 \mu\text{m}^2$ ) for the  $\text{Bi}_2\text{Te}_3$  and  $\text{MnBi}_2\text{Te}_4$  thin films, respectively. The images are presented using a shading effect that highlights step-like features, such as the triangular terraces that are typical of  $\text{Bi}_2\text{Te}_3$  samples,<sup>20</sup> as shown in Fig. 2(b). These triangular structures are also observed on the surface of the  $\text{MnBi}_2\text{Te}_4$  film, as shown in Fig. 2(c), but lack distinct steps and reach a height of up to 20 nm. The presence of triangular shapes on the surface indicates regions where adatoms have less mobilities and thus form clusters, already observed in others van der Waals materials.<sup>24</sup> The van der Waals growth mode allows growth with good out-of-plane orientation even in a large mismatch substrate such as cubic GaAs. However, the in-plane rotation responsible for the defects observed in the RSM can be easily identified by the misalignment of the triangular features shown in Fig. 2(a, b) and (e, f) for  $\text{Bi}_2\text{Te}_3$  and  $\text{MnBi}_2\text{Te}_4$ , respectively. The red dotted lines in HRTEM images of Fig. 2(c) and (g) indicate the quintuple layer (QL) of  $\text{Bi}_2\text{Te}_3$  and the septuple layer (SL) of  $\text{MnBi}_2\text{Te}_4$ . Fig. 2(d) and (h) are higher resolution images showing details of the QL (Te-Bi-Te-Bi-Te) and SL (Te-Bi-Te-Mn-Te-Bi-Te) separated by the van der Waals gap, which form the  $\text{Bi}_2\text{Te}_3$  and  $\text{MnBi}_2\text{Te}_4$  structures, respectively.

From reflection (003)- $\text{Bi}_2\text{Te}_3$  and (006)- $\text{MnBi}_2\text{Te}_4$  obtained from HRXRD data and estimates using data from HRTEM, the value estimated for the QL thickness was approximately 1.0 nm, while that for the SL was approximately 1.4 nm. These results were in good agreement with other experimental results.<sup>20,25</sup>

STM and STS measurements were conducted to investigate the surface electronic properties of the  $\text{Bi}_2\text{Te}_3$  and  $\text{MnBi}_2\text{Te}_4$  thin films. In a typical STS curve, the differential tunneling conductance ( $dI/dV$ ) is proportional to the local density of states (LDOS) at the STM tip position;<sup>26</sup> therefore, it allows us to probe the presence of topological surface states on the MBE grown thin film surface.

A comparison between the LDOS of  $\text{Bi}_2\text{Te}_3$  and  $\text{MnBi}_2\text{Te}_4$  is presented in Fig. 3. Fig. 3(a) shows a series of  $dI/dV$  curves (shaded blue region) taken along a line scan with different positions on the  $\text{Bi}_2\text{Te}_3$  surface at room temperature, superposed with the average  $dI/dV$  curve (solid blue line). In all measured spectra, the region of positive bias voltage denotes the bulk conduction band (BCB) and the region of negative bias voltage denotes the bulk valence band (BVB), thus confirming a homogenous behavior of  $\text{Bi}_2\text{Te}_3$  LDOS throughout the sample surface. The presence of a finite density of states near the Fermi energy ( $E_F = 0$ ) that varies linearly with the bias voltage is a signature of topologically protected surface states, confirming the topological properties of MBE-grown  $\text{Bi}_2\text{Te}_3$  thin films.<sup>26–29</sup> Moreover, by extrapolating the linear region of the  $dI/dV$  curve to the zero conductance axis, it is possible to

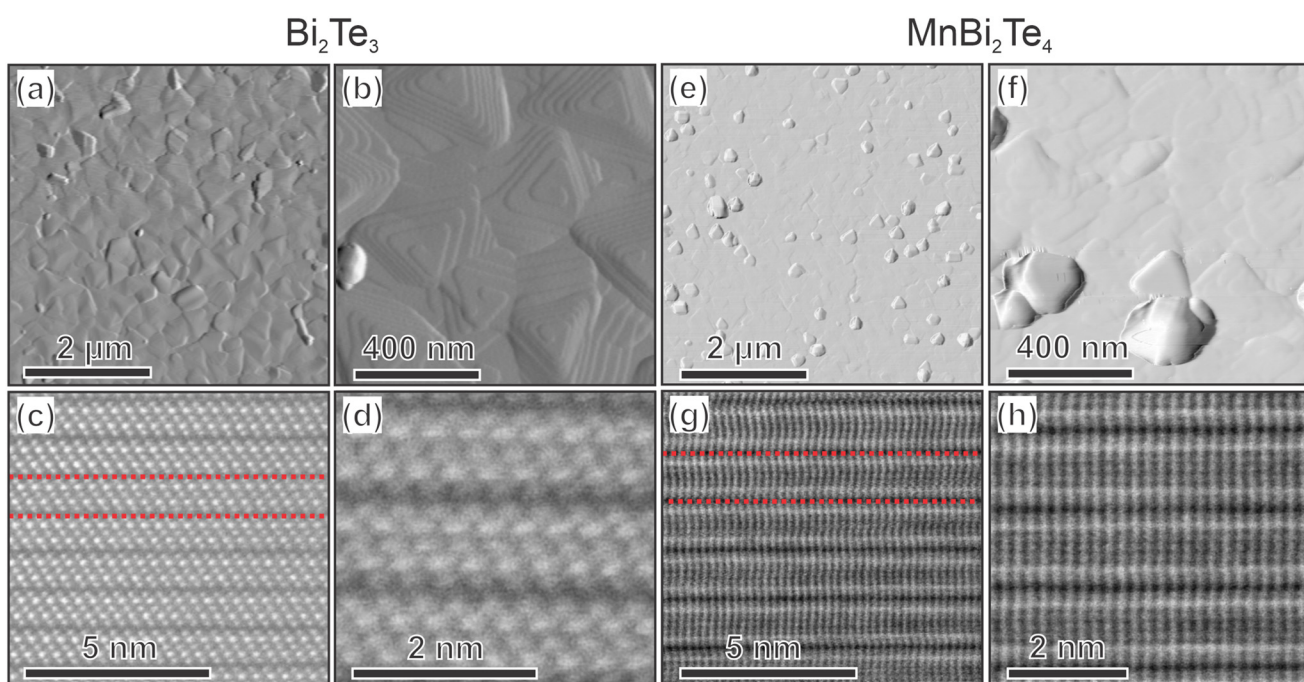
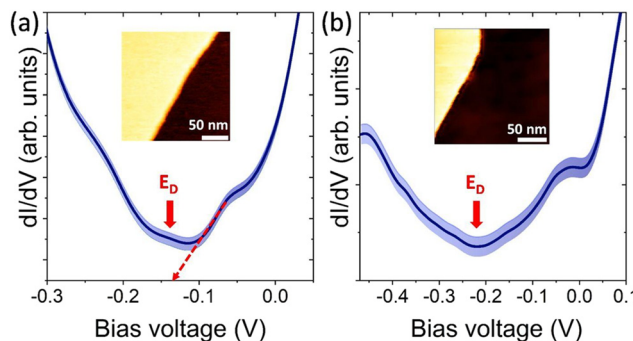


Fig. 2 (a and b) AFM surface and (c and d) HRTEM images of  $\text{Bi}_2\text{Te}_3$  thin films. The triangular structures with flat terraces and observable steps corresponding to the quintuple layers of  $\text{Bi}_2\text{Te}_3$  are clearly shown in (b). (e and f) AFM surface and (g and h) HRTEM images of  $\text{MnBi}_2\text{Te}_4$  thin films.  $\text{MnBi}_2\text{Te}_4$  exhibits a smoother surface with grains and flat triangle structures. The maximum peak height  $S_p$  (which corresponds to the maximum height with respect to the mean height) for AFM images (a), (b), (e), and (f) are 24 nm, 16 nm, 110 nm and 75 nm, respectively. The red dotted line corresponds to the (c)  $\text{Bi}_2\text{Te}_3$  quintuple layers and (g)  $\text{MnBi}_2\text{Te}_4$  septuple layers.



**Fig. 3** A series of  $dI/dV$  spectra (shaded blue region) and spatially averaged  $dI/dV$  curve (solid blue line) obtained along the  $\text{Bi}_2\text{Te}_3$  (a) and  $\text{MnBi}_2\text{Te}_4$  surface (b). In both graphs, the zero- bias voltage represents the Fermi level ( $E_F$ ) and the red arrow denotes the Dirac point energy ( $E_D$ ). In panel (a), the linear conductance region (dashed red line) indicates the presence of topological surface states (TSSs). Inset shows the STM topographic image where the STS curves were measured, evidencing the QL termination of  $\text{Bi}_2\text{Te}_3$  and the SL termination of  $\text{MnBi}_2\text{Te}_4$  with step heights of 1.01 and 1.35 nm, respectively. STM images were acquired using  $I = 400$  pA and  $V = 0.8$  V.

obtain a Dirac point energy ( $E_D$ ) of  $-190$  meV, which indicates a lightly n-type doping character of  $\text{Bi}_2\text{Te}_3$  thin films. Fig. 3(b) shows an averaged  $dI/dV$  curve (solid blue line) taken along different points on the  $\text{MnBi}_2\text{Te}_4$  surface (blue shaded region). In this case, the topological properties of MBE-grown  $\text{MnBi}_2\text{Te}_4$  thin films can be confirmed by the presence of a finite density of states from  $-0.3$  eV to the Fermi level ( $E_F = 0$ ), where the  $E_D$  is obtained considering the minimum of the  $dI/dV$  curve as already been reported in STS measurements in  $\text{MnBi}_2\text{Te}_4$  bulk single crystals and thin films.<sup>27,30</sup> Because the  $\text{Bi}_2\text{Te}_3$  growth parameters are the starting point to obtain  $\text{MnBi}_2\text{Te}_4$  with correct stoichiometry, the STS curve indicates that the n-type doping is still present in the  $\text{MnBi}_2\text{Te}_4$  phase with the Dirac point located around  $-210$  meV below the Fermi level. Indeed, since at room temperature, antiferromagnetic ordering is not expected to occur, time-reversal symmetry is preserved at the surface of  $\text{MnBi}_2\text{Te}_4$ , maintaining its topological properties.<sup>27</sup> The value for the QL ( $\text{Bi}_2\text{Te}_3$ ) and SL ( $\text{MnBi}_2\text{Te}_4$ ) measured *via* STM, as shown in the insets of Fig. 3(a) and (b), was 1.01 nm and 1.35 nm, respectively, in agreement with those mentioned previously.

To prove the possibility of integrating  $\text{MnBi}_2\text{Te}_4$  with group II-VI semiconductors with epitaxial quality, 60 nm thick CdTe was grown on the top of  $\text{MnBi}_2\text{Te}_4$  as an insulating cap layer owing to its high resistivity. The HRXRD of this sample is shown in Fig. 4(a). With the exception of the CdTe film reflections known and labeled by CdTe(111) and CdTe(222), all others are identical to those depicted in Fig. 1(f). The film growth aligned with the 00L planes of  $\text{MnBi}_2\text{Te}_4$  and showed high crystalline quality. The growth dynamics of the zinc blende crystal CdTe layer on top of the van der Waals material has not been studied; however, it is remarkable that a highly crystalline CdTe layer can be grown onto the  $\text{MnBi}_2\text{Te}_4$  film with such a large lattice mismatch. The RSM around CdTe

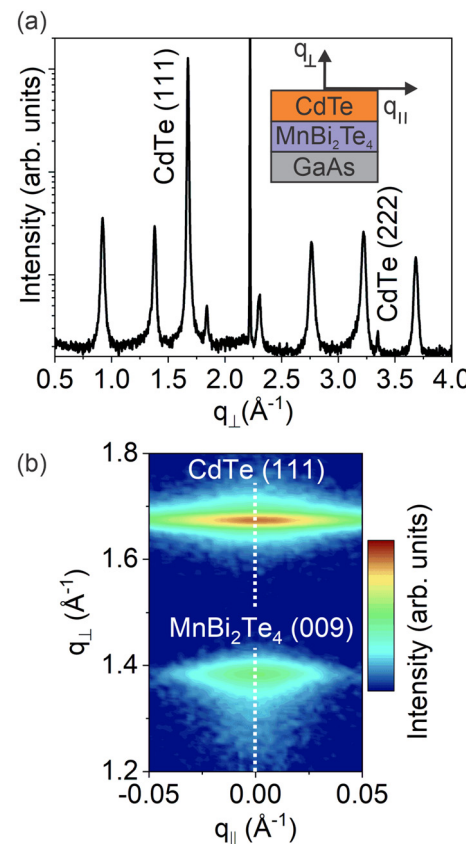


**Fig. 4** (a) HRXRD and (b) reciprocal map of the GaAs/ $\text{MnBi}_2\text{Te}_4$ /CdTe heterostructure.

(111) and  $\text{MnBi}_2\text{Te}_4$ (009) was performed and is shown in Fig. 4(b). The Bragg diffraction peak displays a broader peak in the in-plane direction for the CdTe(111) and  $\text{MnBi}_2\text{Te}_4$ (009) peaks. The scattering along the crystal truncation rod of CdTe (111) is symmetrical, contrary to  $\text{MnBi}_2\text{Te}_4$ (009), which is larger for in-plane smaller values.

In Fig. 5, we present the results of electrical and magneto-transport measurements for the  $\text{MnBi}_2\text{Te}_4$  thin film with a the CdTe cap layer (Fig. 4). As CdTe is highly resistive (usually  $R_{\text{CdTe}} > 100$  M $\Omega$ ), it does not contribute to the measurements. A schematic of the measurement configuration is shown in the inset of Fig. 5(a). Longitudinal electric resistance ( $R_{xx}$ ) as a function of temperature is shown in Fig. 5(a), showing the antiferromagnetic transition temperature that manifests as a peak in the  $R_{xx}$  around 19 K. As this value is very close to values reported in the literature for a few SL layers of  $\text{MnBi}_2\text{Te}_4$  exfoliated flakes<sup>16,25</sup> and for thin films grown *via* MBE on Si (111),<sup>14</sup> it is not clear whether the CdTe cap layer or defects could play some role in the critical temperature of this transition. At low temperatures ( $< 10$  K), one observes an increase in  $R_{xx}$  as the temperature is decreased. This is explained by localization effects caused by disorder in the crystal. Moreover, the metallic behavior of the  $R_{xx}(T)$  curve (Fig. 5(a)) shows that electrical transport occurs *via* the  $\text{MnBi}_2\text{Te}_4$  layer; otherwise, one would observe a semiconductor-like behavior instead of

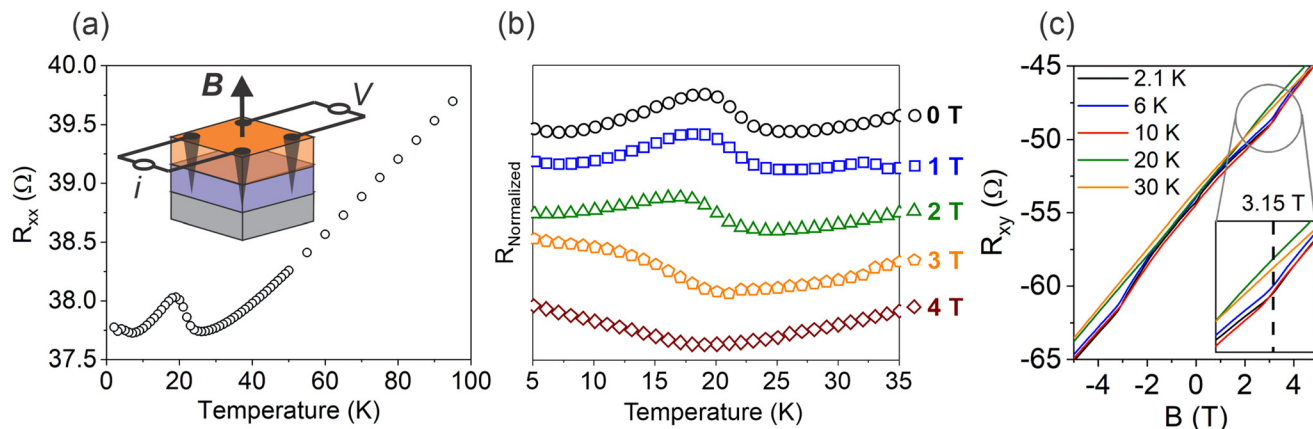


**Fig. 5** (a) Electrical resistance as a function of temperature, where the AFM transition is clear around 19 K. The inset illustrates the diffusion of indium through the CdTe layer until it reaches the MnBi<sub>2</sub>T<sub>4</sub> film, forming ohmic contact for the measurements. (b) Normalized electrical resistance as a function of temperature for different applied magnetic fields, where it is possible to observe the suppression of the AFM transition for higher fields. (c) The transversal electrical resistance showing a transition from AFM to FM for  $B > 3T$ .

metallic behavior. Fig. 5(b) shows normalized electrical resistance as a function of temperature for different applied magnetic fields. For clarity, the curves were shifted. The applied magnetic field dislocates the transition to lower temperatures, as expected, because the applied magnetic field tends to suppress antiferromagnetic alignment. It is also possible to observe that the transition is suppressed for  $B > 3T$ . Fig. 5(c) presents the transversal electrical resistance ( $R_{xy}$ ) as a function of the applied magnetic field. At high temperatures, 20 and 30 K, one observes the linear behavior expected for a single channel transport in this system.<sup>31</sup> However, for lower temperatures, 2.1, 6 and 10 K, a dip in the  $R_{xy}$  curves around 3T is clearly observed. In this temperature region, the sample is already in the antiferromagnetic state. The dip in the  $R_{xy}$  curves indicates that for  $B > 3T$ , the sample suffers a transition from antiferromagnetic to ferromagnetic.

## Conclusions

In summary, we studied MnBi<sub>2</sub>Te<sub>3</sub> thin layers with topological insulator and ordered magnetic properties. High-quality MnBi<sub>2</sub>Te<sub>3</sub> layers were obtained on GaAs(001) substrates using a recently published Bi<sub>2</sub>Te<sub>3</sub> growth recipe<sup>20</sup> by adding only Mn with an effusion cell to achieve the correct MnBi<sub>2</sub>Te<sub>4</sub> stoichiometry. A CdTe layer was used as a cap layer with high epitaxial quality and integration potential with the II-VI semiconductor group through van der Waals growth. Moreover, the metallic behavior of the electrical resistance curve shows that the CdTe cap layer was successfully integrated, thus exhibiting a clean and noise-free signal. GaAs has consolidated industrial fabrication processes and is commonly utilized in existing optical-electronic devices. The integration of MnBi<sub>2</sub>Te<sub>4</sub> thin films on the GaAs substrate with II-VI semiconductors establishes a path to intrinsic magnetic topological insulator devices based on the integration between van der Waals materials.

## Author contributions

Wesley F. Inoch, Sukarno O. Ferreira and Leonarde N. Rodrigues were responsible for the growth of MnBi<sub>2</sub>Te<sub>4</sub> via MBE and conducted HRXRD and reciprocal map measurements. Gilberto Rodrigues-Junior and Ângelo Malachias were responsible for STM and STS measurements. S. L. A. Mello carried out AFM measurements. S. de Castro and M. L. Peres carried out transport measurements. Bráulio S. Archanjo, Maybi F. Sampaio and Olavo Teixeira Neto conducted the HRTEM measurements.

## Data availability

Data are available upon request from the authors.

## Conflicts of interest

There are no conflicts to declare.

## Acknowledgements

We acknowledge the financial support by the Brazilian funding agencies CAPES, CNPq (under Grant 408093/2022-6), and FAPEMIG (under Grant APQ-02500-22, APQ-00388-22 and RED-00223-23).

## References

- 1 M. Z. Hasan and C. L. Kane, *Rev. Mod. Phys.*, 2010, **82**, 3045–3067.

2 M. König, S. Wiedmann, C. Brüne, A. Roth, H. Buhmann, L. W. Molenkamp, X.-L. Qi and S.-C. Zhang, *Science*, 2007, **318**, 766–770.

3 O. Breunig and Y. Ando, *Nat. Rev. Phys.*, 2021, **4**, 184–193.

4 B. A. Bernevig, C. Felser and H. Beidenkopf, *Nature*, 2022, **603**, 41–51.

5 Y. Tokura, K. Yasuda and A. Tsukazaki, *Nat. Rev. Phys.*, 2019, **1**, 126–143.

6 Y. Deng, Y. Yu, M. Z. Shi, Z. Guo, Z. Xu, J. Wang, X. H. Chen and Y. Zhang, *Science*, 2020, **367**, 895–900.

7 D. Zhuo, Z.-J. Yan, Z.-T. Sun, L.-J. Zhou, Y.-F. Zhao, R. Zhang, R. Mei, H. Yi, K. Wang, M. H. W. Chan, C.-X. Liu, K. T. Law and C.-Z. Chang, *Nat. Commun.*, 2023, **14**, 7596.

8 C.-Z. Chang, J. Zhang, X. Feng, J. Shen, Z. Zhang, M. Guo, K. Li, Y. Ou, P. Wei, L.-L. Wang, Z.-Q. Ji, Y. Feng, S. Ji, X. Chen, J. Jia, X. Dai, Z. Fang, S.-C. Zhang, K. He, Y. Wang, L. Lu, X.-C. Ma and Q.-K. Xue, *Science*, 2013, **340**, 167–170.

9 Q. Li, S.-K. Mo and M. T. Edmonds, *Nanoscale*, 2024, **16**, 14247–14260.

10 M. M. Otrokov, I. P. Rusinov, M. Blanco-Rey, M. Hoffmann, A. Yu Vyazovskaya, S. V. Eremeev, A. Ernst, P. M. Echenique, A. Arnau and E. V. Chulkov, *Phys. Rev. Lett.*, 2019, **122**, 107202.

11 Y. Bai, Y. Li, J. Luan, R. Liu, W. Song, Y. Chen, P.-F. Ji, Q. Zhang, F. Meng, B. Tong, L. Li, Y. Jiang, Z. Gao, L. Gu, J. Zhang, Y. Wang, Q.-K. Xue, K. He, Y. Feng and X. Feng, *Natl. Sci. Rev.*, 2023, **11**, 1–9.

12 Y. Li, C. Liu, Y. Wang, Z. Lian, S. Li, H. Li, Y. Wu, H.-Z. Lu, J. Zhang and Y. Wang, *Sci. Bull.*, 2023, **68**, 1252–1258.

13 P. Kagerer, C. I. Fornari, S. Buchberger, S. L. Morelhão, R. C. Vidal, A. Tcakaev, V. Zabolotnyy, E. Weschke, V. Hinkov, M. Kamp, B. Büchner, A. Isaeva, H. Bentmann and F. Reinert, *J. Appl. Phys.*, 2020, **128**, 135303.

14 N. Liu, S. Schreyeck, K. M. Fijalkowski, M. Kamp, K. Brunner, C. Gould and L. W. Molenkamp, *J. Cryst. Growth*, 2022, **591**, 126677.

15 J. Lapano, L. Nuckols, A. R. Mazza, Y.-Y. Pai, J. Zhang, B. Lawrie, R. G. Moore, G. Eres, H. N. Lee, M.-H. Du, T. Z. Ward, J. S. Lee, W. J. Weber, Y. Zhang and M. Brahlek, *Phys. Rev. Mater.*, 2020, **4**, 111201.

16 Y.-F. Zhao, L.-J. Zhou, F. Wang, G. Wang, T. Song, D. Ovchinnikov, H. Yi, R. Mei, K. Wang, M. H. W. Chan, C.-X. Liu, X. Xu and C.-Z. Chang, *Nano Lett.*, 2021, **21**, 7691–7698.

17 S.-K. Bac, K. Koller, F. Lux, J. Wang, L. Riney, K. Borisiak, W. Powers, M. Zhukovskiy, T. Orlova, M. Dobrowolska, J. K. Furdyna, N. R. Dilley, L. P. Rokhinson, Y. Mokrousov, R. J. McQueeney, O. Heinonen, X. Liu and B. A. Assaf, *npj Quantum Mater.*, 2022, **7**, 46.

18 A. Koma, *Thin Solid Films*, 1992, **216**, 72–76.

19 M. Tanaka, *J. Cryst. Growth*, 2005, **278**, 25–37.

20 L. N. Rodrigues, C. I. L. de Araujo, S. L. A. Mello, J. Laverock, J. M. Fonseca, W. Schwarzacher, W. F. Inoch and S. O. Ferreira, *J. Appl. Phys.*, 2023, **134**, 085301.

21 A. K. Ray, R. Swan and C. A. Hogarth, *J. Non-Cryst. Solids*, 1994, **168**, 150–156.

22 L. G. Parratt, *Phys. Rev.*, 1954, **95**, 359–369.

23 J. Als-Nielsen and D. McMorrow, *Elements of Modern X-ray Physics*, Wiley, 2011.

24 M. He, Y. Fu, Y. Huang, H. Sun, T. Guo, W. Lin, Y. Zhu, Y. Zhang, Y. Liu, G. Yu and Q. L. He, *J. Phys.: Condens. Matter*, 2023, **35**, 295701.

25 Y. Li, Y. Wang, Z. Lian, H. Li, Z. Gao, L. Xu, H. Wang, R. Lu, L. Li, Y. Feng, J. Zhu, L. Liu, Y. Wang, B. Fu, S. Yang, L. Yang, Y. Wang, T. Xia, C. Liu, S. Jia, Y. Wu, J. Zhang, Y. Wang and C. Liu, *Nat. Commun.*, 2024, **15**, 3399.

26 H. Beidenkopf, P. Roushan, J. Seo, L. Gorman, I. Drozdov, Y. S. Hor, R. J. Cava and A. Yazdani, *Nat. Phys.*, 2011, **7**, 939–943.

27 H. Kim, M. Liu, L. Frammolino, Y. Li, F. Zhang, W. Lee, C. Dong, Y.-F. Zhao, G.-Y. Chen, P.-J. Hsu, C.-Z. Chang, J. Robinson, J. Yan, X. Li, A. H. MacDonald and C.-K. Shih, *ACS Appl. Nano Mater.*, 2024, **7**, 21149–21159.

28 C. Parra, T. H. Rodrigues da Cunha, A. W. Contryman, D. Kong, F. Montero-Silva, P. H. Rezende Gonçalves, D. D. Dos Reis, P. Giraldo-Gallo, R. Segura, F. Olivares, F. Niestemski, Y. Cui, R. Magalhaes-Paniago and H. C. Manoharan, *Nano Lett.*, 2017, **17**, 97–103.

29 G. Rodrigues-Junior, T. Chagas, R. Reis, P. V. Sciammarella, C. I. Fornari, P. H. O. Rappl, E. Abramof, R. Magalhães-Paniago and Á. Malachias, *Phys. Rev. B*, 2023, **108**, 035408.

30 J.-Q. Yan, Q. Zhang, T. Heitmann, Z. Huang, K. Y. Chen, J.-G. Cheng, W. Wu, D. Vaknin, B. C. Sales and R. J. McQueeney, *Phys. Rev. Mater.*, 2019, **3**, 064202.

31 J. Cui, M. Shi, H. Wang, F. Yu, T. Wu, X. Luo, J. Ying and X. Chen, *Phys. Rev. B*, 2019, **99**, 155125.